

Nitrogen Codoped Unique Carbon with 0.4 nm Ultra-Micropores for Ultrahigh Areal Capacitance Supercapacitors

HPSTAR
626-2018

Junshuang Zhou, Li Hou, Sunrui Luan, Jinlong Zhu, Huiyang Gou, Dong Wang, and Faming Gao*

A full understanding of ion transport in porous carbon electrodes is essential for achieving effective energy storage in their applications as electrochemical supercapacitors. It is generally accepted that pores in the size range below 0.5 nm are inaccessible to electrolyte ions and lower the capacitance of carbon materials. Here, nitrogen-doped carbon with ultra-micropores smaller than 0.4 nm with a narrow size distribution, which represents the first example of electrode materials made entirely from ultra-microporous carbon, is prepared. An in situ electrochemical quartz crystal microbalance technique to study the effects of the ultra-micropores on charge storage in supercapacitors is used. It is found that ultra-micropores smaller than 0.4 nm are accessible to small electrolyte ions, and the area capacitance of obtained sample reaches the ultrahigh value of $330 \mu\text{F cm}^{-2}$, significantly higher than that of previously reported carbon-based materials. The findings provide a better understanding of the correlation between ultra-micropore structure and capacitance and open new avenues for design and development of carbon materials for the next generation of high energy density supercapacitors.

1. Introduction

Supercapacitors are promising devices for applications requiring rapid pulses of energy or high power with rapid repetitive recharging owing to their exceptional power density and cyclability compared with those of Li batteries.^[1–8] Electrical double-layer capacitors (EDLCs) store energy by adsorbing anions and cations at an electrode/electrolyte interface on the surface of highly porous materials. The double-layer capacitance resulting from electrostatic charge storage is in the range of $10\text{--}25 \mu\text{F cm}^{-2}$ and no Faradic reactions occur at the

EDLC. To achieve a higher energy storage capacity, research efforts are currently focused on optimizing the pore structure and introducing heteroatoms into carbon materials to enhance the capacitance of EDLCs.^[9–11]

The introduction of heteroatoms, such as N, O, B, and F, onto the surface or into the bulk of the carbon materials, is considered to be a promising approach to improving the specific capacitance and energy density of carbon materials.^[12–16] Heteroatoms that provide a pair of electrons can modulate the electron donor–acceptor characteristics of carbon materials and create additional functional groups on the carbon surface. These effects can considerably enhance the capacitance of carbon electrodes by contributing an additional pseudocapacitance in the form of surface Faradaic reactions.^[17,18] In recent years, nitrogen-

doped carbon materials have emerged as the most promising candidates for alternative electrode materials for EDLC applications owing to their excellent performance.^[19–23] Recently, Lin et al.^[23] developed a nitrogen-doped ordered mesoporous few-layer carbon with a high specific surface area ($1580 \text{ m}^2 \text{ g}^{-1}$) and a very high nitrogen doping concentration (12 at% nitrogen doping), which displayed a record gravimetric capacitance of 855 F g^{-1} in aqueous electrolytes.

Gogotsi et al.^[24] synthesized carbide derived carbon (CDC) with unimodal micropores of $0.6\text{--}2.25 \text{ nm}$ for EDLCs. These tailored sub-nanoporous carbons exhibited very high capacitances in an organic electrolyte. Following this study, the origin of the anomalous increase in capacitance has received considerable attention. It has been shown that the maximum volumetric capacitance was achieved when the carbon pore size matched that of the adsorbing electrolyte ions.^[25–29] The development of in situ experimental techniques, including the electrochemical quartz crystal microbalance^[30–32] (EQCM) and small-angle X-ray scattering^[33–35] (SAXS), has radically modified understanding of charge storage mechanisms and ion dynamics in nanoporous carbon-based supercapacitors in aqueous electrolytes. Recently, Prehal et al.^[33] used SAXS to characterize ion adsorption mechanisms in confined pores and the effects of different microporous carbons on the capacitance. Their results showed that the

Dr. J. Zhou, Prof. L. Hou, Dr. S. Luan, Prof. H. Gou, Dr. D. Wang, Prof. F. Gao
Key Laboratory of Applied Chemistry
College of Environmental and Chemical Engineering
Yanshan University
Qinhuangdao 066004, P. R. China
E-mail: fmgao@ysu.edu.cn
Prof. J. Zhu, Prof. H. Gou
Center for High Pressure Science and Technology Advanced Research
Beijing 100094, China

 The ORCID identification number(s) for the author(s) of this article can be found under <https://doi.org/10.1002/sml.201801897>.

DOI: 10.1002/sml.201801897

pore size of the carbon material decreased from 1.3 to 0.65 nm, while the volumetric capacitance considerably increased from 80 to 180 F cm⁻³. Thus, ionic transport in microporous electrodes is an important consideration for energy storage in electrochemical supercapacitors. Studies on the effects of the pore size on capacitance could enable further performance improvements by maximizing the electrode surface area accessible to the electrolyte ions.^[36–41] However, to date, no studies have examined effects of micropores smaller than 0.4 nm on the performance of electrochemical capacitors. Moreover, it has yet to be determined whether ultra-micropores of the nitrogen-enriched carbon materials can affect the pseudocapacitance of the materials.

In this work, we successfully synthesized nitrogen codoped carbon microspheres (CM), with unimodal 0.3–0.4 nm nanopores, by a simple low-temperature solvothermal route without postprocessing. We used in situ EQCM measurements to directly reveal the effects of the ultra-micropores (i.e., pores smaller than 0.4 nm) on charge storage in supercapacitors. This is the first example of a supercapacitor made from a unimodal ultra-microporous carbon electrode material. We showed that the ultra-micropores were accessible to small electrolyte ions and enabled fast diffusion of electrolyte ions at the surface and in the bulk. The nitrogen doping induced a pseudocapacitance by improving the mobility of negative charges on the carbon surfaces. The synergic effects of the ultra-micropores and nitrogen doping enabled carbon microspheres with a gravimetric capacitance up to 147 F g⁻¹ in H₂SO₄. Moreover, when the ultra-micropore total volume of the carbon microspheres increased from 0.006 to 0.016 cm³ g⁻¹, the gravimetric capacitance increased from 147 to 294 F g⁻¹. More importantly, due to the narrow size distribution of ultra-microporous carbon than typical carbon-based electrodes, the area capacitance of obtained sample reaches the value of 330 μF cm⁻², significantly higher than that of previously reported electrode materials.^[23,43–46] This work provides a better understanding of the correlation between ultra-microporous structures and their capacitance. We present a new strategy for designing better supercapacitors with optimized carbon pore sizes in future applications.

2. Structural Features and Composition

Low-magnification scanning electron microscope (SEM) images of the nitrogen-doped carbon microspheres and carbon microspheres without nitrogen (CM-X) (Figure 1 and Figure S1, Supporting Information) showed that the samples consisted of microspheres and a spherical geometry ≈4 and 12 μm, respectively. An enlarged image (inset) further illustrates the smooth surface and near-perfect spherical geometry of the samples. The doping of nitrogen into the carbon microspheres was detected by energy-dispersive X-ray (EDX) spectroscopy. We confirmed the presence of C and N in the nitrogen-doped carbon microspheres (Table S2, Supporting Information). A high-magnification SEM image of the samples and the corresponding elemental mappings (Figure 1c–eh) indicated that both C and N were distributed uniformly throughout the entire area of the samples.

We compared the structures of the samples by collecting X-ray diffraction (XRD) patterns. As shown in Figures S2a and S3a (Supporting Information), two broadened diffraction peaks were observed at 2θ of 26.2° and 43.8°, analogous to the (002) and (101) planes of graphite. The broadening of the peaks suggested the possible presence of an amorphous carbon phase within the carbon spheres. For the carbon microsphere synthesized with diethylamine (CM-D) and carbon microsphere synthesized with acetonitrile (CM-A), the broad peak corresponding to the graphite-like (002) showed a similar intensity for both samples, which suggested the graphitization. Raman spectra (Figures S2b and S3b, Supporting Information) showed a G-band at 1601 cm⁻¹ and a typical D-band located at 1372 cm⁻¹, attributed to the vibration of sp² bonded carbon atoms in a 2D hexagonal lattice and disordered carbon atoms with defects, respectively. The intensity ratio *I*_D/*I*_G (1.02) of CM-D was close to that of CM-A (1.03), indicating a similar crystal structure for the two samples, consistent with the XRD results.

The pore structure of the samples was further investigated by N₂ adsorption measurements. The Barrett–Emmett–Teller (BET) surface area and pore volume calculated by the quenched solid density functional theory (QSDFT) method are summarized in Figure S4 and Table S1 (Supporting Information). The samples displayed a typical type II isotherm based on the adsorption/desorption isotherms. This type of isotherm is characteristic of nonporous solid materials, which may have surface area inaccessible to nitrogen adsorption. The low adsorption amount suggested a very low surface area as calculated from the N₂ adsorption (1–2 m² g⁻¹). However, the quadrupole moment of the N₂ molecule limits access of the gas to small pores at 77 K. Thus, N₂ sorption cannot accurately reflect the porosity values of ultra-micropores (<0.7 nm).^[21,40–42] To further examine the ultra-micropore structure of the samples, we used CO₂ adsorption at 273.2 K and synchrotron radiation small-angle X-ray scattering (SAXS) to assess the surface area of the ultra-micropores with size less than 1 nm (Figure 2a–d). The presence of ultra-micropores in the size range of 0.34–0.38 nm was indicated by the CO₂ sorption data (Figure 2b,c), and the total pore volumes of 0.016 and 0.006 cm³ g⁻¹ for CM-D and CM-A, respectively. The adsorption behavior of the CMs was unclear possibly owing to the low surface interaction with the CO₂ molecules. Porosity measurements with data from SAXS are shown in Figure 2d. The pore size distribution was computed from the SAXS data to show ultra-micropores with sizes in the range of 0.3–0.4 nm in the samples. The higher peak intensity suggested a higher porosity in CM-D than that of CM-A, which was in good qualitative agreement with the CO₂ adsorption measurements.

Elemental chemical environments in the samples were further investigated by X-ray photoelectron spectroscopy (XPS) (Figure 3). We found a similar pattern with a predominant narrow graphitic C 1s peak at 284.6 eV and small peaks at 398.8 and 532.3 eV. The presence of an O 1s peak at 532 eV in the sample could be attributed to partial surface oxidation.^[41] Quantitative elemental analysis indicated a high doping content of nitrogen in CM-D (11.89 wt%) and CM-A (12.43 wt%), respectively (see Table S2, Supporting Information). The complex N 1s spectra could be further deconvoluted into three different peaks at binding energies of 398.3, 399.8, and 400.7 eV, attributable to

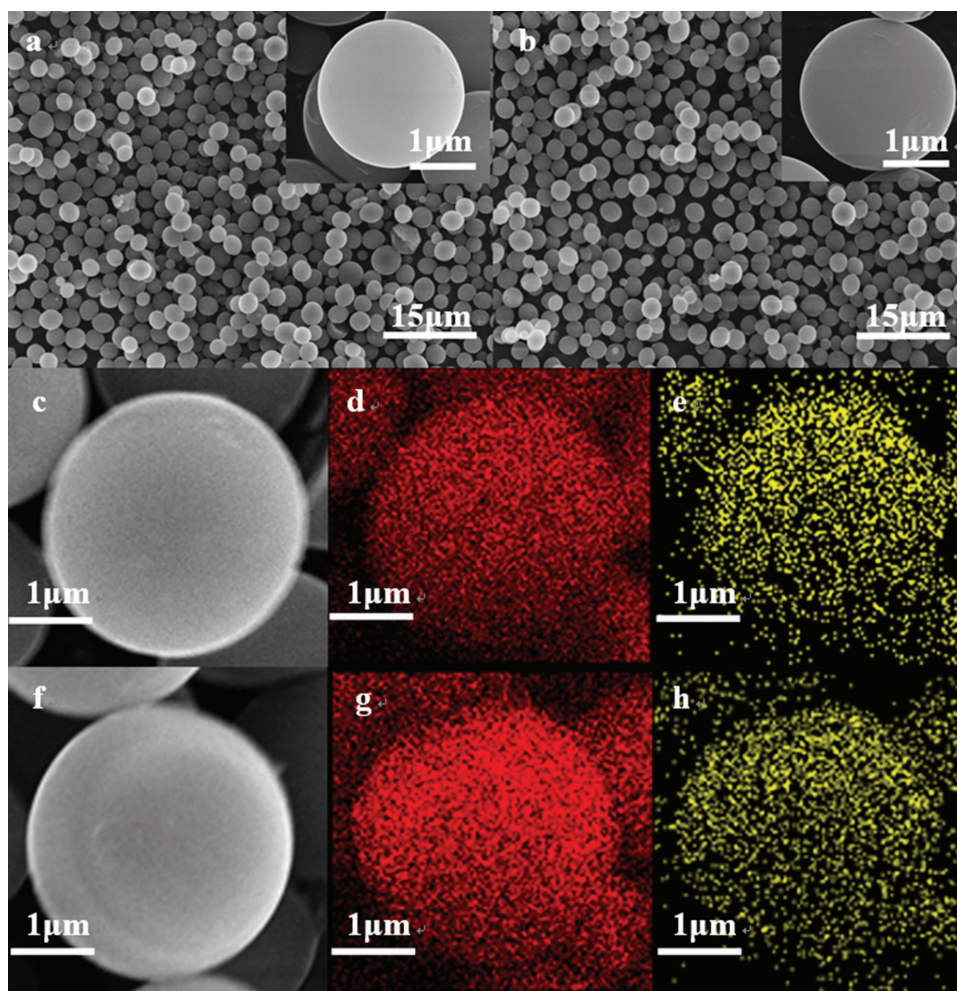


Figure 1. Morphology and elemental distribution of the carbon microspheres: a) low-magnification SEM image of the CM-D (inset: high-magnification SEM image); b) low-magnification SEM image of the CM-A (inset: high-magnification SEM image); c) SEM image of CM-D, and d,e) corresponding EDS elemental maps of carbon (red) and nitrogen (yellow); f) SEM image of CM-A, and g,h) corresponding EDS elemental maps of carbon (red) and nitrogen (yellow). Scale bars: 15 μm (a, b), 1 μm (a, b, inset), and 1 μm (c, d, e, f, g, h).

pyridinic, pyrrolic, and graphitic nitrogen atoms, respectively. Pyridinic N (N1) atoms were located at the edges of the graphitic planes, bonded to two carbon atoms and hybridized with one p-electron in the aromatic system. Pyrrolic-N (N2) atoms bonded with two carbon atoms and contributed to the p system with two p-electrons. Graphitic N atoms were incorporated into the graphene layer and substituted carbon atoms within the graphene plane. However, the high-resolution N1s spectra (Figure 3 and Table S3, Supporting Information), indicated differences in the shapes of these three peaks between the two different samples and different amounts of the N bonding configurations formed in the carbon microspheres.

3. Electrochemical Performance

To further study the influence of the ultra-micropore structure on the electrochemical properties, the samples were simultaneously characterized by cyclic voltammetry (CV) and EQCM in 1 M H_2SO_4 aqueous solutions. Figure 4a,b demonstrates the

characteristic capacitive behavior with rectangular CV profiles, thus, confirming the results of a previous study^[42] conducted with the samples showing that both cations and anions could freely access the sub-0.4-nm pores. Figure 4a,b shows the relationship between frequency and potential; according to the Sauerbrey equation, the frequency (Δf) response decreases when the electrode mass (Δm) increases. In this potential range, an increase of the electrode mass observed during the negative scan was associated with cation adsorption; during the positive scan, the electrode mass decrease corresponded to desorption. The periodic mass change of the CM-D electrode during cycling was much higher than that of the CM-A electrode. This result clearly indicated that adsorption of both cations and anions was related to the ultra-microporous volume of the electrode. Figure 4c shows the results of the CM without ultra-micropores tested in 1 M H_2SO_4 . Owing to the lack of an ultra-microporous structure in the CM, we expected ions to have limited access to the electrodes. Indeed, no mass change of the quartz was observed upon cycling, as previously shown by other groups.^[30,42] Both the CV and EQCM results further

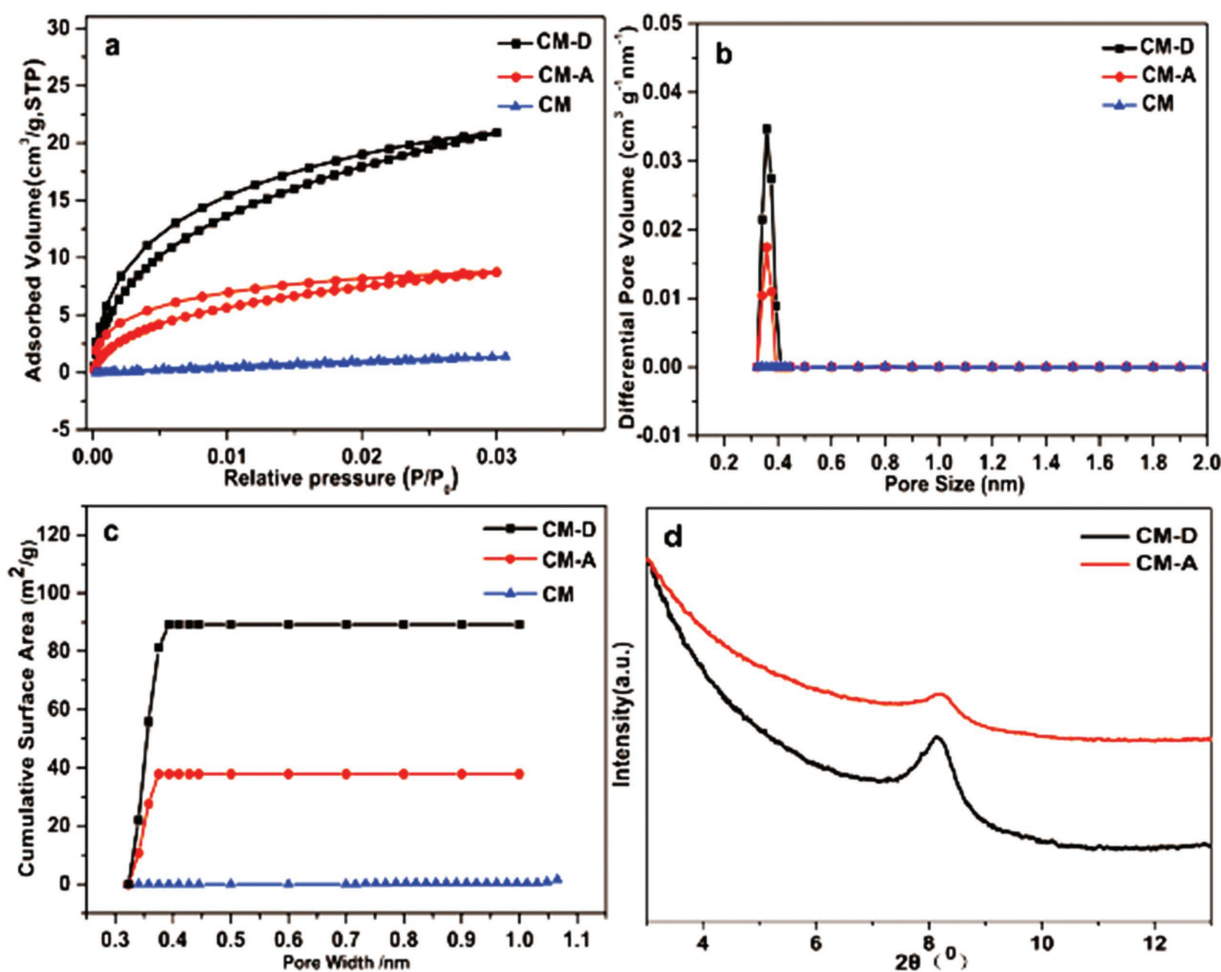


Figure 2. Adsorption behaviors and surface characteristics of the carbon microspheres: a) CO₂ (273.2 K) isotherm; b) pore size distributions for CO₂; c) cumulative specific surface area; d) small-angle X-ray scattering (SAXS) patterns of synthesized carbon microspheres.

confirmed that the ultra-micropores (<0.4 nm) allowed penetration of small ions, such as H⁺. This effect may have enhanced the ionic transport behavior during electrochemical testing and contributed to the considerably improved electrochemical performance.

To evaluate the electrochemical performance of the samples as EC electrodes, we applied the CMs as working electrodes in a 1 M H₂SO₄ aqueous electrolyte solution at a scan rate of 5 mV s⁻¹ using a three-electrode setup with a saturated calomel electrode (SCE) reference electrode. Cyclic voltammograms

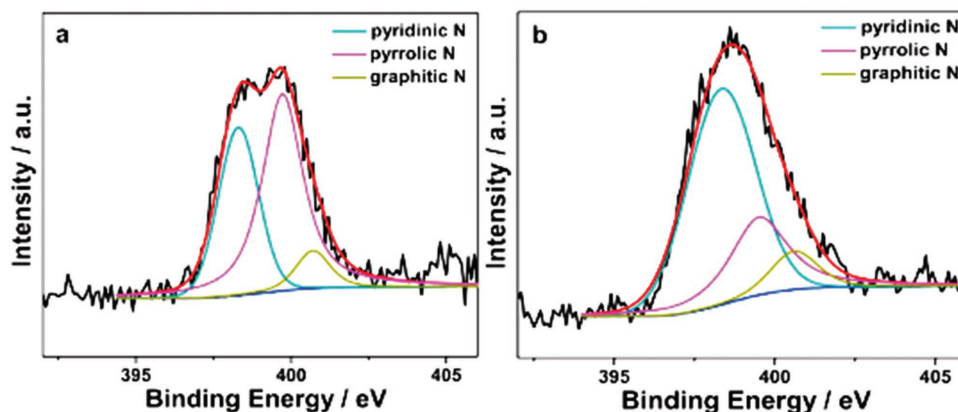


Figure 3. Chemical analysis of the carbon microspheres: a) high-resolution XPS spectra of N1s, of CM-D; b) high-resolution XPS spectra of N1s, of CM-A.

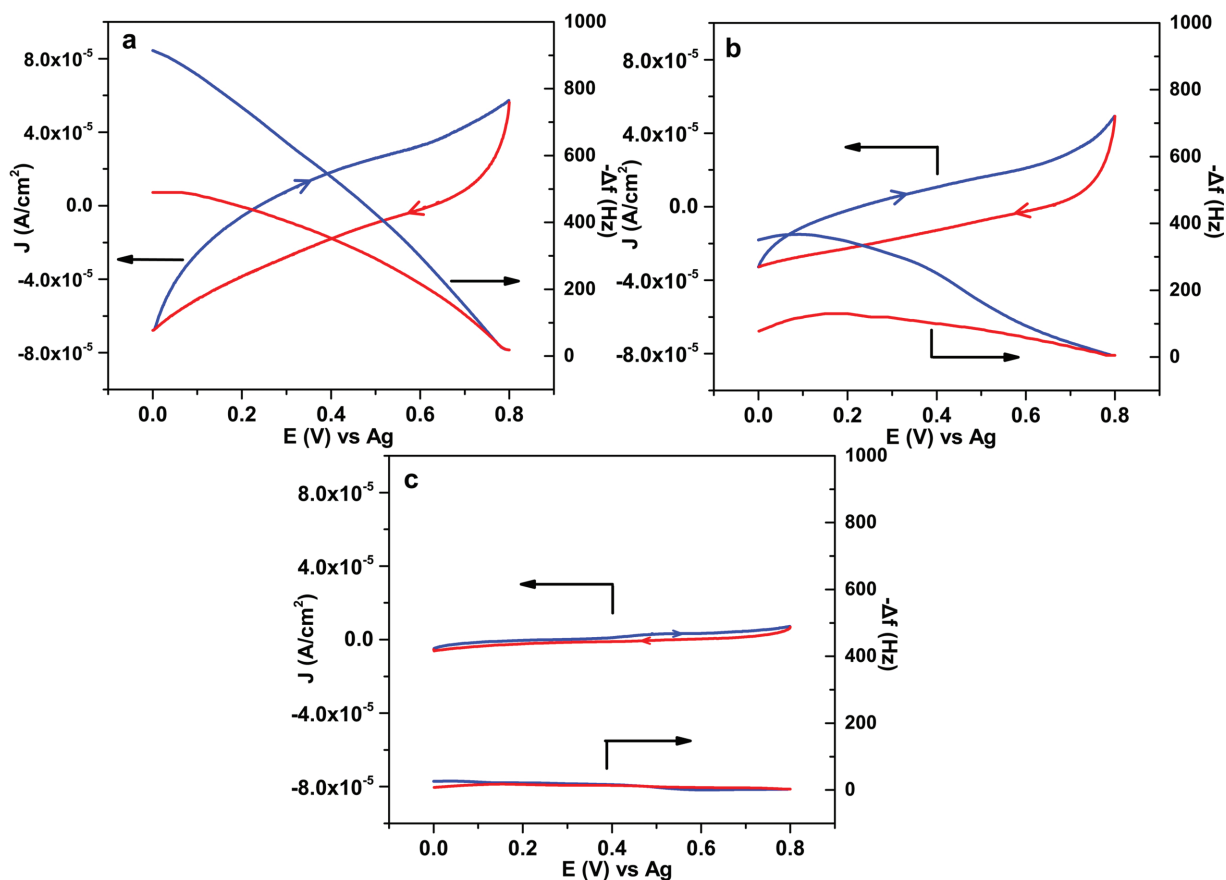


Figure 4. In situ measurements of ionic diffusion in the carbon microspheres: a–c) CV and EQCM frequency response of CM-D, CM-A, and CM, in 1 M H₂SO₄ solution at a scan rate of 5 mV s⁻¹.

(Figure 5a) exhibited a small rectangular curve and very low capacitances for the CMs owing to the extremely low pore volume and lack of nitrogen doping. The samples doped with nitrogen, presented a typical shape with distinct pseudocapacitive behavior over a wide voltage range of -0.1 to 0.6 V (vs SCE). This result could be attributed to Faradaic redox reactions, as observed in cyclic voltammetry plots. A distinct pair of broad and overlapping redox peaks was more clearly observed in the CV curve for CM-D than in that of the CM-A sample. Thus, the greatly increased capacitance can be attributed to the large ultra-micropore volume of CM-D. These results indicated that the ultra-micropores (less than 0.4 nm) within the carbon spheres enhanced the ionic transport behavior and participated in the pseudocapacitance reaction, improving the electrochemical performance of electrodes.

The redox reactions could also be observed in galvanostatic charge/discharge curves (Figure 5b), in which a nonlinearity occurred, representative of the pseudocapacitive behavior of the samples. A small transition in the line slopes around 0.5 V in acidic solution correlated with the redox peaks in the CV curves. Thus, the existence of the ultra-micropores greatly improved the specific capacitance of carbon microsphere electrodes, as calculated from the charge/discharge curves. The specific capacitance of CM-D was calculated to be 294 F g⁻¹ at a current density of 0.1 A g⁻¹, which was much higher than that of the CM-A (147 F g⁻¹) and CM-X (16.2 F g⁻¹), and two orders

of magnitude greater than that of the CMs without heteroatom doping (2 F g⁻¹). The excellent electrochemical performance of the sample might be attributed to the presence of ultra-micropores (<0.4 nm) provided an adequate ion-accessible surface area for charge accommodation, and allow penetration of small ions, that is, H₃O⁺, have similar size within the range 2.82 Å, into the entire volume of the active materials. And by comparing the pore size distribution and charge/discharge results, we can conclude that a little larger total ultra-micropore volume of CM-D (0.016 cm³ g⁻¹) than that of CM-A (0.006 cm³ g⁻¹) contributed to a much greater gravimetric capacitance of 147 versus 294 F g⁻¹. For such pore diameter, a slightly increasing coverage of the inner ultra-micropore is more suitable to the ion coming in and out from the pore channel. And due to the ultra-microporous carbon possesses a much lower surface area than other typical carbon-based electrodes (1500 – 2000 m² g⁻¹), the area-normalized capacitance (C_a , μF cm⁻²) of the CM-D electrode is up to 330 μF cm⁻² at 0.1 A g⁻¹, significantly higher than those from carbon-based electrodes, such as activated carbons (10 – 25 μF cm⁻²),^[43] carbide-derived carbons (5 – 22 μF cm⁻²),^[44] MXene-derived carbons (24 μF cm⁻²),^[45] nitrogen-enriched carbon materials (73.4 μF cm⁻²),^[46] and functionalized graphene sheets (54.1 μF cm⁻²).^[23]

To assess the performance of our nitrogen-doped carbon microsphere electrode in the context of the literature, the best results reported for nitrogen-doped carbon-based electrodes

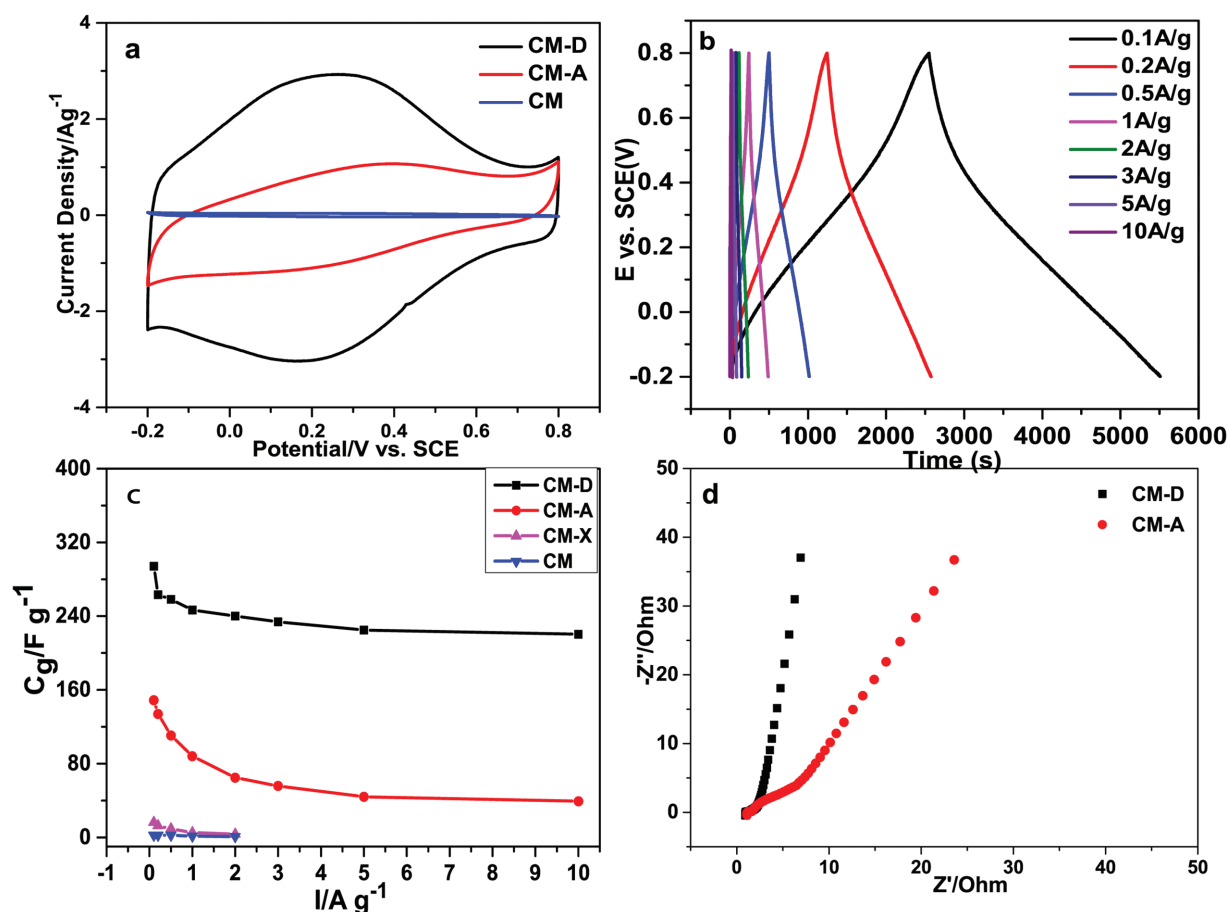


Figure 5. Electrochemical performance of the carbon microspheres: a) CV curves of CM, CM-D, and CM-A samples in 1 M H₂SO₄ solution at a scan rate of 5 mV s⁻¹; b) galvanostatic charge/discharge curves of CM-Ds samples in 1 M H₂SO₄ solution with different current densities; c) corresponding capacity retention at current densities in the range 0.1–10 A g⁻¹; and d) electrochemical impedance spectra under the influence of an ac voltage of 5 mV.

are listed in Table S4 (Supporting Information). In this table, we compare the major characteristics of surface area, total volume, electrolyte, normalized capacitances, and the rate capability. Clearly, the area-normalized capacitance (C_a , $\mu\text{F cm}^{-2}$) of CM-D is much higher than that of previously reported nitrogen-doped carbon-based materials. The outstanding electrochemical performance of the CM-D might be attributed to a combination of two factors: first, the nitrogen doping greatly enhanced the capacitance of the carbon electrodes owing to the pseudocapacitance effect; second, the presence of ultra-micropores (<0.4 nm) provided an adequate ion-accessible surface area for charge accommodation. As shown in the previous studies,^[17–19] nitrogen-containing functional groups play a crucial role in inducing pseudocapacitance by improving the charge mobility of the carbon and introducing negative charges on the carbon surface. These effects result in ion doping/dedoping, similar to that observed in conducting polymers. The presence of a relatively large amount of electrochemically active pyridine N and pyrrolic N (Table S3, Supporting Information) was confirmed in the XPS spectrum (Figure 3). The pyrrolic N likely played an important role in enhancing the specific capacitance. This presumption is supported by theoretical studies of Strelko et al.^[47] and Zhu et al.^[48] Their quantum chemical calculations showed that pyrrole nitrogen improves

charge mobility in a carbon matrix by introducing electron-donor characteristics and by enhancing the carbon catalytic activity for electron-transfer reactions. Moreover, for the first time, we used in situ EQCM measurements to directly show that ultra-micropores were accessible to small electrolyte ions and allowed fast penetration of ions into the entire volume of the active material. The accessibility of ions enabled Faradaic reactions at both the surface and in the bulk of the CMs. A sharp increase in capacitance with decreasing pore size was reported in the studies of Gogotsi et al.,^[24] which revealed an anomalous increase in the volumetric capacitance of nanoporous carbons with pore sizes smaller than 1 nm. Therefore, a greater understanding of ionic transport in ultra-microporous carbon electrodes and the ability to control this factor may hold the key to optimizing the gravimetric capacitance and volumetric capacitance performance of supercapacitors for different applications. The larger total ultra-micropore volume of CM-D (0.016 cm³ g⁻¹) than that of CM-A (0.006 cm³ g⁻¹) contributed to a greater gravimetric capacitance of 147 versus 294 F g⁻¹. The packing density showed almost no change, thus the volumetric capacitance of the CM-D was twice as large as that of the CM-A. This result implies that ultra-microporous carbon materials not only allow faster penetration of ions into the numerous effective active sites, but also served as ion-buffering

reservoirs. These features shorten the ion diffusion paths to the interior surfaces, thereby contributing to the excellent capacitive behavior.

Electrochemical impedance spectroscopy (EIS) was performed to further investigate the ion-transport behavior and electrical resistance of the supercapacitor. We used the samples as the electrodes over a frequency range of 0.01 Hz to 1 MHz (Figure 5d). The steeper slope of CM-D than that of CM-A in the low-frequency region of the EIS spectra confirmed that its higher capacitive behavior was a result of the larger ultra-micropore volume and nitrogen doping. The semicircle at high frequency became much smaller for the CM-D, indicating much better electrochemical capacitive properties, lower diffusion resistance, and lower charge transfer resistance for the CM-D than for the CM-A. The greatly improved charge transfer efficiency was responsible for the superior performance of the doped electrodes in mitigating capacitance fading at a higher current density (over 226 F g⁻¹ for CM-D vs ≈40 F g⁻¹ for the CM-A).

An ideal supercapacitor should be able to deliver the same energy under any operation conditions. Therefore, it is important to investigate the capacitance retention at higher current densities. As shown in Figure 5b, the CM-D electrode also exhibited an excellent rate capability. The specific capacity maintained an extremely high value above 226 F g⁻¹ at a high current density of 10 A g⁻¹ in 1 M H₂SO₄, and the capacitance retention remained ≈75% as the current density was increased from 0.1 to 10 A g⁻¹ (Figure 5c). However, the specific capacitance of the CM-A decreased rapidly from 147 to 40 F g⁻¹ when the current density was increased from 0.1 to 10 A g⁻¹. Thus, it could be that access to pores smaller than 0.4 nm is slightly hampered in a high current density, it may also indicate that there may be some resistance in the process of rapid ion conduction in ultra-micropores. In addition, the pore structure of ultra-micropores has little effect on the electrochemical double-layer capacitance, which mainly increases the pseudocapacitance of the electrode material. A long cycling life is another important requirement for supercapacitors. We studied the durability of the CM-D electrode with galvanostatic charge/discharge measurements to characterize the long-term charge/discharge behavior at a current density of 5 A g⁻¹. As shown in Figure S5 (Supporting Information), the electrode exhibited excellent electrochemical stability with no loss of the initial specific capacitance after 10 000 cycles in H₂SO₄, indicating the excellent long-term stability of the electrode. We observed a gradual increase of the capacitance, which was likely attributed to continuous diffusion of electrolyte ions into the ultra-micropores. Furthermore, active processes at the electrode likely contributed to a gradual increase in the amount of effective charge storage sites in the CM-D electrode and thus the specific capacitance.

4. Conclusion

In summary, we demonstrate an effective strategy for designing high-performance electrodes with a high capacitance based on ultra-micropores smaller than 0.4 nm. We used cyclic voltammetry with in situ EQCM measurements to directly reveal the effect of the ultra-micropores on charge storage in the

supercapacitors. The measured mass changes showed that the small electrolyte ions could easily access the ultra-micropores with 0.3–0.4 nm pores, which is reported for the first time in the field of supercapacitors. Moreover, the carbon microspheres only with the ultra-micropores achieved an ultrahigh areal capacitance up to 330 μF cm⁻² in H₂SO₄, and exhibited an excellent electrochemical stability with no loss of the specific capacitance over 10 000 cycles in acid solution. More importantly, these findings open up new avenues for development and design of heteroatom-enriched carbon materials for the next generation of high energy density supercapacitors.

5. Experimental Section

Materials Synthesis: The carbon microspheres with nitrogen were prepared by a solvothermal reaction in a stainless-steel autoclave (40 mL in total capacity) under autogenous pressure and in a dry glove box with flowing N₂. In a typical process, a single organic solvent, anhydrous diethylamine (C₄H₁₁N) as the carbon and nitrogen source, was transferred to a stainless-steel autoclave. The autoclave was sealed and maintained at 400 °C for 24 h in a furnace, and then allowed to cool to room temperature naturally. The resulting mixture was collected and washed with distilled water, ethanol, and hydrochloric acid several times to remove impurities. The product CM-D was dried in vacuum at 80 °C for 10 h. The carbon microspheres with nitrogen were synthesized under similar conditions with acetonitrile instead of diethylamine to form CM-A. The carbon microspheres without nitrogen were synthesized under similar conditions with xylene instead of diethylamine to form CM-X. And the CM were purchased from Tianjin BTR New Energy Materials Co., Ltd., China, as control materials for comparison with the performance with the codoped carbon spheres.

Materials Characterization: XRD was measured with the use of a D/max-2500/PC X-ray diffractometer and Cu Kα radiation (λ = 0.15418 nm). Raman spectra of the samples were recorded at room temperature on a WiTec Raman system (Alpha 300) with a 100× objective lens and a 633 nm He-Ne laser. Fluorescence spectra were measured with a Princeton Instruments Spectrograph (SP2750) having a 20× objective and 532 nm excitation source. The morphology and elemental composition were studied with a scanning electron microscope (JEOL JSM 7001F SEM) operating at an accelerating voltage of 5 kV with energy dispersive X-ray spectroscopy (Oxford-Horiba Inca XMax50 EDX). The XPS measurements were performed on a PHI QUANTERA-II SXM X-ray Photoelectron Spectrometer. The N₂ adsorption analysis was conducted on a TriStar 3020 accelerated surface area system equipped with an automated surface area at 77 K based on BET calculations for the surface area. The CO₂ isotherms were recorded at 273.2 K with a Micromeritics ASAP 2460. The pore size distribution curves were obtained from the adsorption branch isotherms by a density functional theory method. SAXS experiments were collected at the B1 station of CHESS, USA. Diffraction was collected at room temperature at an X-ray wavelength of 0.486282 Å for 400 s. A CeO₂ sample was used for the calibration and Mar345 was used as the detector, with a sample-to-detector distance of ≈890 mm. The 2D diffraction pattern was converted to 1D with the use of FIT2D software. The data were collected over a scattering vector Q, where Q = 4πsinθ/λ = 2π/d, θ is the scattering angle, λ is the X-ray wavelength, and d is the dimension of a feature in real space.

Electrochemical Measurements: The frequency difference between the working crystal and a reference crystal was measured with an EQCM (Model CHI 440, CHI Instruments). The resonant frequency of the fundamental mode of the reference crystal (f₀) was 8.0 MHz. The correlation between the mass change Δm and the frequency variation Δf was calculated based on the Sauerbrey equation

$$\Delta m = -\frac{A \times \sqrt{\rho \mu}}{2f_0^2} \times \Delta f \quad (1)$$

where Δm is in g, Δf is in Hz, A is the area of the gold working electrode (0.196 cm^2), ρ is the density of quartz (2.684 g cm^{-3}), and μ is the shear parameter of quartz ($2.947 \times 10^{11} \text{ g cm}^{-1} \text{ s}^{-2}$). Substitution of all the parameters into Equation (1) showed that a frequency variation of +1 Hz corresponds to a mass change of -1.36 ng . In a three-electrode system, the sample was used as the test gold electrode with a platinum wire as the counter electrode, and the reference electrode was Ag/AgCl in $1 \text{ M H}_2\text{SO}_4$. CV studies were performed on a CHI 440 electrochemical workstation (Shanghai Chenhua, China) in the potential range of 0–0.8 V versus Ag/AgCl at a scan rate of 5 mV s^{-1} . The current and quartz frequency were simultaneously recorded.

In the three-electrode system, the test electrode was prepared by loading a slurry consisting of 85 wt% active material, 10 wt% carbon black, and 5 wt% poly(vinylidene fluoride) (PVDF) in *N*-methylpyrrolidone onto a Pt-mesh, which was dried at $80 \text{ }^\circ\text{C}$ for 6 h under vacuum and then dried further under vacuum at $100 \text{ }^\circ\text{C}$ for 12 h. The electrodes were obtained by coating an active mass of 2–4 mg onto each current collector (1 cm^2 area). The sample was used as the test electrode with platinum foil as the counter electrode. The reference electrode was a SCE electrode in $1 \text{ M H}_2\text{SO}_4$. CV studies were performed on a CHI 660D electrochemical workstation (Shanghai Chenhua, China) in the potential range of -0.2 to 0.8 V versus SCE at a scan rate of 5 mV s^{-1} . The galvanostatic charge/discharge cycles were measured by a Land cell tester (CT 2001A) at 0.1 – 10 A g^{-1} over a voltage range of -0.2 to 0.8 V versus SCE. The specific capacitance (C_s) of the systems was calculated according to the following equation

$$C_g = \frac{I \times \Delta t}{\Delta V \times m} \quad (2)$$

$$C_a = \frac{C_g}{\text{SSA}} \quad (3)$$

where C_s (F g^{-1}) is the gravimetric specific capacitance, C_a is the area-normalized capacitance, that is, the specific capacitance per specific surface area (SSA), I (A) is the charge/discharge current, ΔV (V) stands for the potential window within the discharge time Δt (s), and m (g) corresponds to the amount of active material on the electrode. All experiments were conducted at room temperature ($25 \pm 1 \text{ }^\circ\text{C}$).

Supporting Information

Supporting Information is available from the Wiley Online Library or from the author.

Acknowledgements

The authors acknowledge financial support from the National Natural Science Foundation of China (Grant Nos. 21371149 and 21671168) and the Natural Science Foundation of Hebei (Grant Nos. B2016203498 and 17964403D).

Conflict of Interest

The authors declare no conflict of interest.

Keywords

area capacitance, nitrogen-doped carbon spheres, supercapacitor, unimodal ultra-micropores

Received: May 18, 2018

Revised: July 16, 2018

Published online:

- [1] P. Simon, Y. Gogotsi, *Nat. Mater.* **2008**, *7*, 845.
- [2] P. Simon, Y. Gogotsi, B. Dunn, *Science* **2014**, *343*, 1210.
- [3] B. Conway, *Electrochemical Supercapacitors: Scientific Fundamentals and Technological Applications*, Kluwer Academic, New York **1999**.
- [4] M. Acerce, D. Voiry, M. Chhowalla, *Nat. Nanotechnol.* **2015**, *40*, 1.
- [5] M. Ghidui, M. R. Lukatskaya, M. Q. Zhao, Y. Gogotsi, M. W. Barsoum, *Nature* **2014**, *516*, 78.
- [6] H. Ji, Z. Xin, Z. Qiao, J. Jung, Y. Zhu, Y. Lu, *Nat. Commun.* **2014**, *5*, 3317.
- [7] Y. X. Xu, Z. Y. Lin, X. Zhong, X. Q. Huang, N. O. Weiss, Y. Huang, X. F. Duan, *Nat. Commun.* **2014**, *5*, 4554.
- [8] J. Zhou, J. Lian, L. Hou, J. Zhang, H. Gou, M. Xia, Y. Zhao, T. A. Strobel, L. Tao, F. Gao, *Nat. Commun.* **2015**, *6*, 8503.
- [9] E. Raymundo-Piñero, K. Kierzek, J. Machnikowski, F. Béguin, *Carbon* **2006**, *44*, 2498.
- [10] H. Itoi, H. Nishihara, T. Kogure, T. Kyotani, *J. Am. Chem. Soc.* **2011**, *133*, 1165.
- [11] X. Ma, L. Gan, M. Liu, P. Tripathi, Y. Zhao, Z. Xu, D. Zhu, L. Chen, *J. Mater. Chem. A* **2014**, *2*, 8407.
- [12] J. Han, L. L. Zhang, S. Lee, J. Oh, K. S. Lee, J. R. Potts, J. Ji, X. Zhao, R. S. Ruoff, S. Park, *ACS Nano* **2013**, *7*, 19.
- [13] I. Tallo, T. Thomberg, H. Kurig, K. Kontturi, A. Janes, E. Lust, *Carbon* **2014**, *67*, 607.
- [14] D. Hulicova-Jurcakova, A. M. Puziy, O. I. Poddubnaya, F. Suárez-García, J. M. Tascón, G. Q. Lu, *J. Am. Chem. Soc.* **2009**, *131*, 5026.
- [15] L. Zhao, L. Z. Fan, M. Q. Zhou, H. Guan, S. Qiao, M. Antonietti, M. M. Titirici, *Adv. Mater.* **2010**, *22*, 5202.
- [16] M. J. Jung, E. Jeong, S. Kim, I. L. Sang, J. S. Yoo, Y. S. Lee, *J. Fluorine Chem.* **2011**, *132*, 1127.
- [17] Z.-S. Wu, K. Parvez, A. Winter, H. Vieker, X. Liu, S. Han, A. Turchanin, X. Feng, K. Müllen, *Adv. Mater.* **2014**, *26*, 4552.
- [18] D. Hulicova-Jurcakova, M. Kodama, S. Shiraiishi, H. Hatori, Z. H. Zhu, G. Q. Lu, *Adv. Funct. Mater.* **2009**, *19*, 1800.
- [19] L. L. Zhang, X. Zhao, H. X. Ji, M. D. Stoller, L. F. Lai, S. Murali, S. McDonnell, B. Cleveger, R. M. Wallace, R. S. Ruoff, *Energy Environ. Sci.* **2012**, *5*, 9618.
- [20] D. Wei, Y. Liu, Y. Wang, H. Zhang, L. Huang, G. Yu, *Nano Lett.* **2009**, *9*, 1752.
- [21] R. Arenal, K. March, C. P. Ewels, X. Rocquefelte, M. Kociak, A. Loiseau, O. Stephan, *Nano Lett.* **2014**, *14*, 5509.
- [22] M. A. Pope, I. A. Aksay, *J. Phys. Chem. C* **2015**, *119*, 20369.
- [23] T. Lin, I.-W. Chen, F. Liu, C. Yang, H. Bi, F. Xu, F. Huang, *Science* **2015**, *350*, 1508.
- [24] J. Chmiola, G. Yushin, Y. Gogotsi, C. Portet, P. Simon, P. L. Taberna, *Science* **2006**, *313*, 1760.
- [25] C. Largeot, C. Portet, J. Chmiola, P. L. Taberna, Y. Gogotsi, P. Simon, *J. Am. Chem. Soc.* **2008**, *130*, 2730.
- [26] D. T. Galhena, B. C. Bayer, S. Hofmann, G. A. Amaratunga, *ACS Nano* **2016**, *10*, 747.
- [27] L. Jiang, L. Sheng, C. Long, T. Wei, Z. Fan, *Adv. Energy Mater.* **2015**, *5*, 1500771.
- [28] M. Salanne, B. Rotenberg, K. Naoi, K. Kaneko, P. L. Taberna, C. P. Grey, B. Dunn, P. Simon, *Nat. Energy* **2016**, *1*, 16070.
- [29] R. Burt, K. Breitsprecher, B. Daffos, P. L. Taberna, P. Simon, G. Birkett, X. S. Zhao, C. Holm, M. Salanne, *J. Phys. Chem. Lett.* **2016**, *7*, 4015.
- [30] M. D. Levi, G. Salitra, N. Levy, D. Aurbach, J. Maier, *Nat. Mater.* **2009**, *8*, 872.
- [31] J. M. Griffin, A. C. Forse, W. Y. Tsai, P. L. Taberna, P. Simon, C. P. Grey, *Nat. Mater.* **2015**, *14*, 812.
- [32] M. D. Levi, S. Sigalov, D. Aurbach, L. Daikhin, *J. Phys. Chem. C* **2013**, *117*, 14876.
- [33] C. Prehal, C. Koczwara, N. Jäckel, A. Schreiber, M. Burian, H. Amenitsch, M. A. Hartmann, V. Presser, O. Paris, *Nat. Energy* **2017**, *2*, 16215.

- [34] C. Prehal, D. Weingarth, E. Perre, R. T. Lechner, H. Amenitsch, O. Paris, V. Presserb, *Energy Environ. Sci.* **2015**, *8*, 1725.
- [35] S. Boukhalfa, L. He, Y. B. Melnichenko, G. Yushin, *Angew. Chem., Int. Ed.* **2013**, *52*, 4618.
- [36] C. Merlet, B. Rotenberg, P. A. Madden, P. L. Taberna, P. Simon, Y. Gogotsi, M. Salanne, *Nat. Mater.* **2012**, *11*, 306.
- [37] A. C. Forse, J. M. Griffin, C. Merlet, J. Carreterogonzalez, A. R. O. Raji, N. M. Trease, C. P. Grey, *Nat. Energy* **2017**, *2*, 16216.
- [38] S. Kondrat, P. Wu, R. Qiao, A. A. Kornyshev, *Nat. Mater.* **2014**, *13*, 387.
- [39] A. C. Forse, J. M. Griffin, C. Merlet, P. M. Bayley, H. Wang, P. Simon, C. P. Grey, *J. Am. Chem. Soc.* **2015**, *137*, 7231.
- [40] C. Merlet, C. Péan, B. Rotenberg, P. A. Madden, B. Daffos, P.-L. Taberna, P. Simon, M. Salanne, *Nat. Commun.* **2013**, *4*, 2701.
- [41] S. Boukhalfa, D. Gordon, L. He, Y. B. Melnichenko, N. Nitta, A. Magasinski, G. Yushin, *ACS Nano* **2014**, *8*, 2495.
- [42] W. Y. Tsai, P. L. Taberna, P. Simon, *J. Am. Chem. Soc.* **2014**, *136*, 8722.
- [43] P. Simon, Y. Gogotsi, *Acc. Chem. Res.* **2013**, *46*, 1094.
- [44] M. Oschatz, L. Borchardt, K. Pinkert, S. Thieme, M. R. Lohe, C. Hoffmann, M. Benusch, F. M. Wisser, C. Ziegler, L. Giebeler, M. H. Rummeli, J. Eckert, A. Eychmüller, S. Kaskel, *Adv. Energy Mater.* **2014**, *4*, 105.
- [45] J. Wang, J. Tang, B. Ding, V. Malgras, Z. Chang, X. Hao, Y. Wang, H. Dou, X. Zhang, Y. Yamauchi, *Nat. Commun.* **2017**, *8*, 15717.
- [46] L. F. Chen, Y. Lu, L. Yu, X. W. Lou, *Energy Environ. Sci.* **2017**, *10*, 1777.
- [47] V. V. Strelko, V. S. Kuts, P. A. Throver, *Carbon* **2000**, *38*, 1499.
- [48] J. Zhu, A. S. Childress, M. Karakaya, S. Dandeliya, A. Srivastava, Y. Lin, A. M. Rao, R. Podila, *Adv. Mater.* **2016**, *28*, 7185.